ACS SENSORS

Article

Cite This: ACS Sens. 2018, 3, 1392−1400

pubs.acs.org/acssensors

Plasmonic Biosensor Based on Vertical Arrays of Gold Nanoantennas

Stephanie Klinghammer,[†,#] Tino Uhlig,[‡,#] Fabian Patrovsky,[‡] Matthias Böhm,[‡,¶] Julian Schütt,[†] Nils Pütz,[†] Larysa Baraban,[*,†,§] Lukas M. Eng,[‡,§] and Gianaurelio Cuniberti[†,§]

[†]Institute for Materials Science and Max Bergmann Center of Biomaterials, [‡]Institute of Applied Physics, Chair of Experimental Physics/Photophysics, and [§]Center for Advancing Electronics Dresden (cfaed), TU Dresden, 01062 Dresden, Germany

Supporting Information

ABSTRACT: Implementing large arrays of gold nanowires as functional elements of a plasmonic biosensor is an important task for future medical diagnostic applications. Here we present a microfluidic-channel-integrated sensor for the label-free detection of biomolecules, relying on localized surface plasmon resonances. Large arrays (~1 cm^2) of vertically aligned and densely packed gold nanorods to receive, locally confine, and amplify the external optical signal are used to allow for reliable biosensing. We accomplish this by monitoring the change of the optical nanostructure resonance in the presence of biomolecules within the tight focus area above the nanoantennas, combined with a surface treatment of the nanowires for a specific binding of the target molecules. As a first application, we detect the binding kinetics of two distinct DNA strands as well as the following hybridization of two complementary strands (cDNA) with different lengths (25 and 100 bp). Upon immobilization, a redshift of 1 nm was detected; further backfilling and hybridization led to a peak shift of additional 2 and 5 nm for 25 and 100 bp, respectively. We believe that this work gives deeper insight into the functional understanding and technical implementation of a large array of gold nanowires for future medical applications.

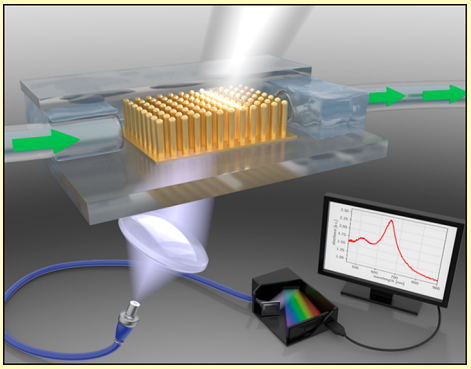

KEYWORDS: *plasmonic biosensors, gold nanowires, nanoantenna, localized surface plasmon resonances (LSPR), DNA biosensor, refractometry, template assisted assembly of nanorods*

The early and personalized detection of diseases, securing food safety, and environmental monitoring are critical societal tasks that demand reliable sensing of biological and chemical species.[1−14] Currently, medical analyses are performed via costly, time-consuming, and laborious analyses, such as enzyme-linked immunosorbent assays,[15−17] polymerase chain reaction,[18−20] electrophoresis,[21,22] and blotting based methods[23,24] that have to be performed in accordingly equipped central laboratories by trained personnel. In these regards, lab-on-chip based biosensor technology based on the use of nanoscopic building blocks can offer an increase of the sensitivity with simultaneous scale down of the whole diagnostic systems, e.g., reaching the size of transportable microchips. Particularly in the field of chemical and bioanalysis, such biosensor platforms are desired for a fast and highly sensitive sample analysis at the point of care (PoC). Taking into account that modern society lives in the era of information technology and the digital revolution that enables access to information on demand, the PoC concept in diagnostics and even medical treatment has strong prospects for further development. In this respect, biosensors based on surface plasmon resonance (SPR) have been attracting interest for decades.[25] SPR sensor platforms offer the possibility for label-free, ultrasensitive, and real-time sensing[26−28] and therefore are a milestone detection technique that is well established, and broadly used. However, commonly available SPR devices are comparably big, complex in their setup, and can require expensive equipment such as preprocessed substrates; so, conventional SPR still suffers in terms of missing capability for point-of-care applications, as it requires miniaturized packaging of the optical system.[29] Long penetration pathways of the molecules limit the size of the sensing area and prevent smaller devices with optimized microfluidic target delivery systems and possibilities from multiplexed sensing.[30] In addition, a reduced sensitivity and poor signals toward small molecules with low molecular weights below 500 g/mol, e.g. steroids, drugs, and toxins, are problematic, too. Usually target labeling or establishments of more complicated competition assays are required to obtain low sensitivities.[31−33]

Propagating surface plasmons usually occurs in continuous metal films, while localized surface plasmons (LSPR) are excited in subwavelength-sized metallic micro- and nanostructures, without the need for extensive optical excitation schemes.[34] Thus, the application of localized surface plasmon resonance sensors helps to extend the limitation of the standard SPR toward the detection of small biomolecules, as well as typically used proteins, antibodies, and other biointeractions. The key element of the efficiency of the LSPR approach is the confined electric field enhancements in

Received: April 20, 2018
Accepted: June 11, 2018
Published: June 11, 2018

Downloaded via BUFFALO STATE on July 28, 2019 at 16:28:08 (UTC).
See https://pubs.acs.org/sharingguidelines for options on how to legitimately share published articles.

© 2018 American Chemical Society

DOI: 10.1021/acssensors.8b00315
ACS Sens. 2018, 3, 1392−1400

the vicinity of the nanostructures.[35,36] Hence LSPR sensors are considered as the next generation of plasmonic based techniques as they have the potential to improve on the last remaining drawbacks of the breakthrough SPR sensors.[37] Previously, most LSPR based sensors[38,27,39] typically required time-consuming and/or expensive top-down fabrication methods, e.g., laborious electron beam or focused ion beam lithography of noble metal nanostructures. Functional structured areas, obtained by this means, are comparably small and thus do not allow for high yield in the measurements. Contrary, bottom up produced structures suffer from defects and heterogeneity limiting the sensing performance, as size and shape of the used nanostructure play together with the latter sensing performance.[40,34] It is certain that nanowires (nanorods) instead of spheres enable higher sensitivities since sharper and narrower peaks in the spectra appear. The spectral positions of the resonances can be tuned by the nanostructure's aspect ratio such that no spectral overlap of the LSPR with the interband transition of gold occurs.[41] Hence, in terms of sensitivity, rods are expected to surpass their propagating counterparts by over 15%.[42,43] Comparison with common high-resolution SPR sensors showed a similar performance of LSPR while having less surface density of interacting molecules.[43] The high demand to track small changes of small molecules in LSPR sensors in a time dependent manner still remains.

The aim of our research is to present a miniaturized concept of a biosensor device that is relying on the large arrays of gold nanoantenna for real-time monitoring of short DNA sequences (below 100 bp) within a reasonable limit of detection (Figure 1a). Therefore, it is essential to design a sensor offering a high number of binding sites and having an integrated fluidic target delivery system. We propose to use vertically aligned gold nanoantenna arrays with a diameter of 17 nm and a length of 400 nm, fabricated using alumina templates.[49] The method of anodic oxidation of aluminum films itself was already known and used industrially since the beginning of the previous century;[44] however, it was only with the emergence of modern nanoscopic imaging techniques, that its self-ordering properties of nanopores and, thus, the full potential for the upcoming nanotechnology was discovered.[44−47] It allows for the production of large scale (up to several cm^2), uniform, defect poor, and densely packed nanostructure arrays,[48] even on flexible substrates.[50] Variations in length, diameter, and distance assured, thanks to the diversity of the available templates, a broad tuning of the optical resonance properties. The combination of the nanoantenna arrays with the developed microfluidic systems provides a high flow rate of liquids and thus an efficient analyte transport in real time. The targeted structuring of nanorods and tailored channel geometries promises a wide range detection of analytes and being compact at all times. In addition, the device employs a fiber-coupled halogen light source and a compact, fiber-coupled spectrometer for signal readout.

The demonstrated device allows implementation of the arbitrary large arrays of the vertically arranged nanorods as a backbone of the sensor of the biological molecules. Although the use of the nanorods in plasmonic biosensors is not new by itself, our approach allows us to combine the *nanoscopic plasmonic effect* of the single nanoantennas with the *macroscopic readout* of the biosensor, where the multiplexed signal of thousands of the nanostructures is taken into account. In this respect our method is able to offer a reliable solution, not relying on, e.g., the response of the single dissolved nanostructures or lithographically patterned chip. Finally, the presented modular synthesis technique introduces the possibility of easy and cost-efficient design of the biochips at virtually any substrate, including flexible supports, etc.

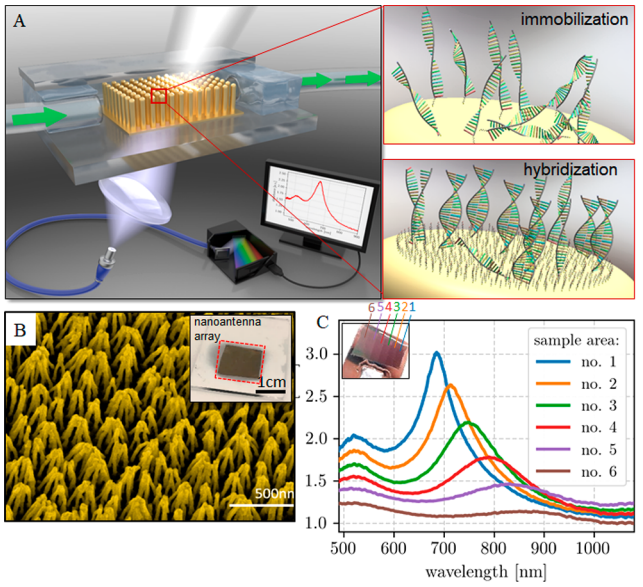

Figure 1. (A) Representative drawing of the LSPR based biosensor for real-time detection: a large array of nanoantennas is incorporated into a microfluidic chamber system that guides analyte solutions precisely over the sensitive area. Optical readout is realized with a spectrometer and spectra are continuously recorded upon chemical reactions; the inset illustrates the investigated biochemical reaction, which is immobilization, backfilling, and hybridization of short DNA sequences. (B) SEM images of vertically aligned nanoantennas. The antennas are homogeneously and densely distributed over the substrate. 400-nm-long and 17-nm-thick rods will be separated from each other when coming into contact with fluids, exhibiting unique LSPR properties in the visible range at λ = 680 nm. The inset shows an image of the substrate after removal of additional titanium layer and aluminum oxide matrix. Comparably big areas can be manufactured fast and easily. (c) Extinction spectra of nanoantennas with different aspect ratios measured at different spots on one and the same sample. The inset shows a photo of the respective sample where the different areas are clearly distinguishable.

We believe that in this realization a biosensor will undoubtedly win from the combination of the nanoscopic nature of the nanorods and its large area that is directly used in the assay. Thus, the integration of the large arrays of nanoantennas into a PoC platform boosts the range of potential applications in the biomedical area. We demonstrate the working platform with the real-time and label-free detection of short oligonucleotide sequences down to low ng/μL range as a precursor for potential water, food, and drug screenings.

EXPERIMENTAL SECTION

Fabrication of Nanoantenna Arrays. Nanoantennas are fabricated via electrochemically driven deposition of gold into nanometer-sized pores of an anodized aluminum oxide (AAO) matrix with the pore diameters in the range of 20 nm. A detailed description of fabrication processes can be found elsewhere.[49] Briefly, sputtering of 5 nm titanium, 8 nm gold, and 300 nm aluminum forms a thin film stack on a glass substrate. Anodizing the aluminum layer at 26 V in a cooled aqueous solution of 0.3 M sulfuric acid at 0 °C results in nanoporous aluminum oxide (AAO). Etching with 0.03 M NaOH for

DOI: 10.1021/acssensors.8b00315
ACS Sens. 2018, 3, 1392−1400

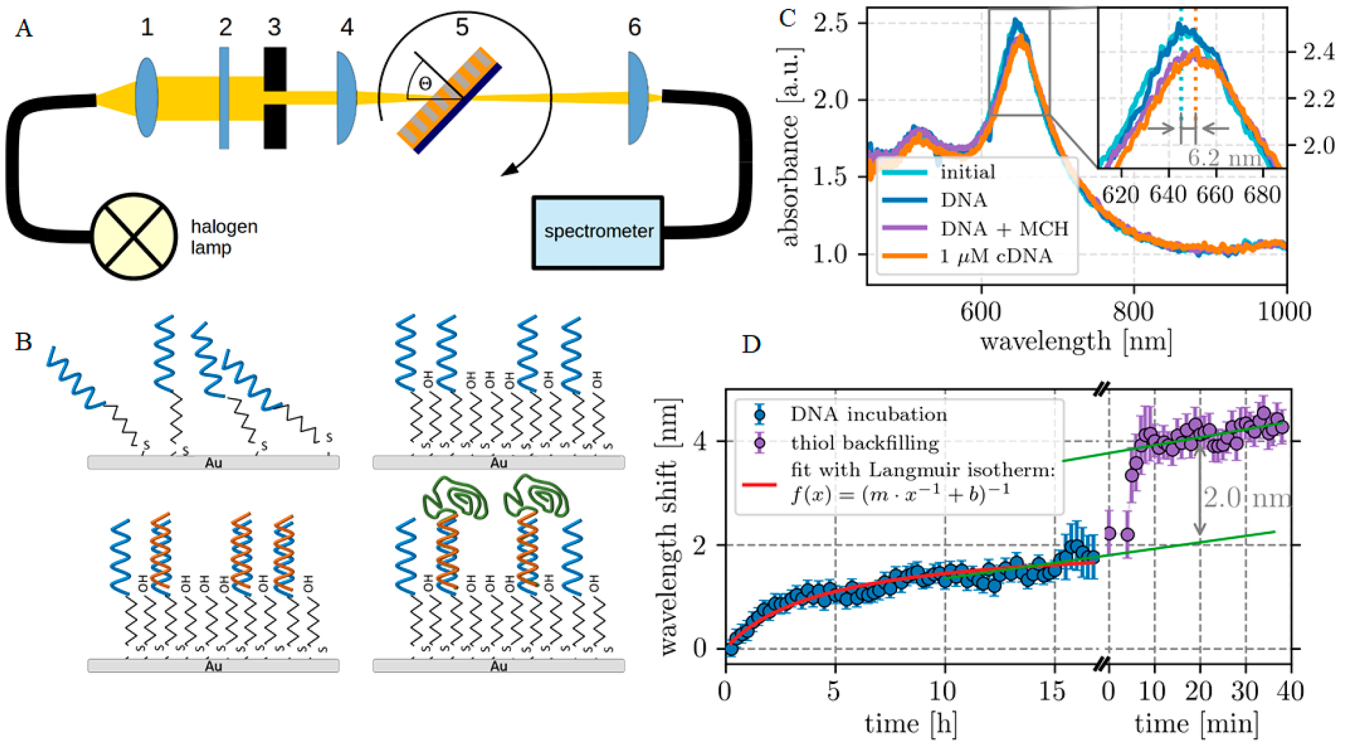

Figure 2. (A) Schematic drawing of the optical setup for measuring transmission spectra of nanorod samples: The white-light beam of a halogen lamp is collimated by a lens (1) and guided through a Glan-Thompson prism (2) for selection of the p-polarized state, whereupon the beam passes a slit aperture (3). The sample itself is placed centrally between two cylindrical lenses (4, 6), where the beam is narrowest, on a rotatable sample holder (5). Eventually, the transmitted light is sent into a fiber-coupled spectrometer. (B) Schematic drawing of the used functionalization approach: first, adsorption of probe DNA onto gold; second, backfilling with MCH; third, hybridization with two different target strands. (C) Optical absorbance spectra of the nanoantenna sample illuminated by p-polarized white light. Two absorbance peaks, at around 530 and 650 nm, are clearly visible in the spectra and correspond to the excitation of the short-axis and the long axis resonance of the nanoantennas, respectively. The inset shows the red-shifts of the long-axis LSPR that follows the different stages of surface functionalization of the nanoantennas. (D) Time-resolved wavelength shift of the long-axis LSPR peak plotted over consecutive stages of immobilization of DNA probe molecules and blocking with mercaptohexanol.

25 s removes the remainder and opens the pores to the bottom gold electrode. The AAO template is filled electrochemically with gold using 0.05 M $HAuCl_4$ (Chempur, Germany), 0.42 M Na_2SO_3, and 0.42 M $Na_2S_2O_3$ (Sigma-Aldrich). Additional etching with 0.03 M NaOH facilitates a complete removal of the surrounding AAO matrix and leaves freestanding gold antennas (Figure 1 b). Resulting nanorods dimensions are 390 nm in length, 17 nm in diameter, and 63 nm interwire spacing (center to center).

SPR and LSPR Setup. Optical absorbance measured on the nanoantennas monitored the excitation of the LSPR (Figure 2 a). The spectral measurements were performed using a rotatable sample holder and a spectrometer (OceanOptics Maya 2000 Pro), while illumination of the sensor was performed by a halogen lamp (LOT-QuantumDesign). The p-polarization was selected by a Glan-Thompson prism in order to suppress background signal from s-polarized light that only excites the short axis resonance. Transmitted light was collected by a fiber and guided to the spectrometer. An angle of incidence of 40° was chosen for maximum signal acquisition. Spectral positions of the long-axis LSPR were calculated via a fitting of the acquired data of the recorded absorbance using two Lorentzian functions as seen in Figure 2c.

Reference experiments on planar gold surfaces were performed by using a surface plasmon resonance spectrometer (Fraunhofer IOF, Jena, Germany) with matching optically transparent TOPAS chips that include integrated micro lenses and a 50-nm-thick gold layer (Capitals, Berlin, Germany). Prior to measurements, the gold area was treated according to the protocols described above. Analyte delivery was maintained under constant temperature at 25 °C and at a flow rate of 10 μL/min.

Biochemical Functionalization of Nanoantennas. After fabrication of the nanoantennas, a surface functionalization was performed (see Figure 2b). All substrates (either gold nanoantenna array or planar gold films) were cleaned by diligent immersion in ethanol, acetone, and double distilled H_2O, for 5 min each, followed by an oxygen plasma treatment (SPI SUPPLY PREP2; USA, 100 W, 0.2 mbar) for 2 min. Immobilization was performed by incubation of 5 or 10 μM of probe DNA in immobilization buffer (IB), which consists of 100 mM potassium phosphate and 10 mM $MgCl_2$ (Fluka Analytical, Germany). Samples were left to rest for up to 16 h in the dark to allow a covalent binding of thiolate probes. Following immobilization, immersion for 30 min in 5 mM 6-mercapto-1-hexanol solution in H_2O (MCH, 97% purity, Sigma-Aldrich) blocked the remaining free surface sites.

Prior to hybridization with complementary DNA strands, the substrates were washed with hybridization buffer (HB), which is 10 mM Tris(hydroxymethyl)aminomethane (TRIS-Base, Fluka Analytical, Germany) and 20 mM $MgCl_2$ at a pH of 7.4. Hybridization with complementary DNA occurred via exposing the structures to complementary DNA strands in HB for 15 min up to 24 h. All three modification steps with both types of target are visualized in Figure 2b. Here, the concentration of complementary DNA strands ranged from 1 nM to 1 μM. Hybridization experiments were all carried out at a constant flow rate of 10 μL/min, adapted with a high accuracy pump (Harvard Apparatus; Mo. Pump 11 Pico Plus Elite, Holliston, USA).

The studied probe−target system consists of a 25-bp-long 5′-thiol-modified probe oligonucleotide (probe DNA), a 25 bp fully complementary strand (cDNA25) as well as a 100 bp partially complementary strand (cDNA100). A 25 bp noncomplementary

DOI: 10.1021/acssensors.8b00315
ACS Sens. 2018, 3, 1392−1400

DNA strand was used as control. All oligonucleotides were purchased from Biomers (Ulm, Germany). The exact sequences are given in Table 1, the underlined sections represent complementary parts. The

Table 1. Oligonucleotide Sequences Used during Experiments[a]

name	sequence (5′-3′)
probe	HS-C6-ATA GGC TCT GCG GAA TAA GGT CTC G
$cDNA_{25}$	CGA GAC CTT ATT CCG CAG AGC CTA T
$cDNA_{100}$	AG GTG GCT CAG GTG CGC CAT AGG TCC CGC ACC TGA GCC ATA TAT GGC TCA GGT GCG CCA TAG GTG GCC ATA GGT T CGA GAC CTT ATT CCG CAG AGC CTA T
control	ATG CGT ACG TGT TGG AGG ACG TAA C

[a]Complementary base pairs are underlined.

design of the sequences was computed by help of the algorithm EGNAS, published in ref 51, to prevent interferences such as hairpin structures and to maintain the guanine-cytosine (GC) content at ~50%.

Between hybridization with different targets, the surface was regenerated by rinsing the substrates thoroughly with 500 μL of the following solutions: H_2O, 0.1 M Na_2 EDTA (SigmaAldrich), H_2O, 0.1 M NaOH (Grüssing GmbH Analytika, Germany), H_2O, hybridization buffer.

Microfluidic Integration. Nanoantenna substrates and thin glass slides (VWR, 23 mm, #1.5) were connected to working sensors with polydimethylsiloxane (PDMS) based microfluidic chambers in a layerwise approach as described in ref 52. PDMS was manufactured as presented elsewhere.[53] Briefly, a silicone elastomer and its curing agent were mixed well in the ratio 1:10 (Sylgard 184 and Sylgard 184 silicone elastomer curing agent, Dow Corning, USA). Before pouring the polymer onto a master-substrate and curing at 80 °C, the mixture was degassed for 15 min. O_2 plasma treatment (SPI SUPPLY PREP2; USA) for 10 s followed force activation of surface groups and enabling the covalent bonding between sensor and microfluidic devices. Merged substrates could rest at 65 °C for at least 3 h until further usage.

Analysis of Fluorescent Intensities. We further verify the surface binding of the DNA molecules and compare the measurements to the ones at the planar gold surface. This helped us investigate the surface coverage and hybridization efficiency of DNA on both substrates, as described elsewhere.[54] Planar substrates were fabricated by evaporating 3 nm chromium and 20 nm gold onto freshly cleaned coverslips (Menzel, Ø = 13 mm, #1.5) in a dual source thermal evaporation unit (Leybold UNIVEX 300, Germany). To validate the amount of bound DNA, a set of carboxyfluorescein (FAM)-labeled DNA was immobilized on relevant substrates as described above, followed by immersion of substrates in freshly prepared 12 mM 2-mercaptoethanol (Bio-Rad Laboratories Ltd., UK) solution in 0.3× phosphate buffered saline for 16 h. In contrast,

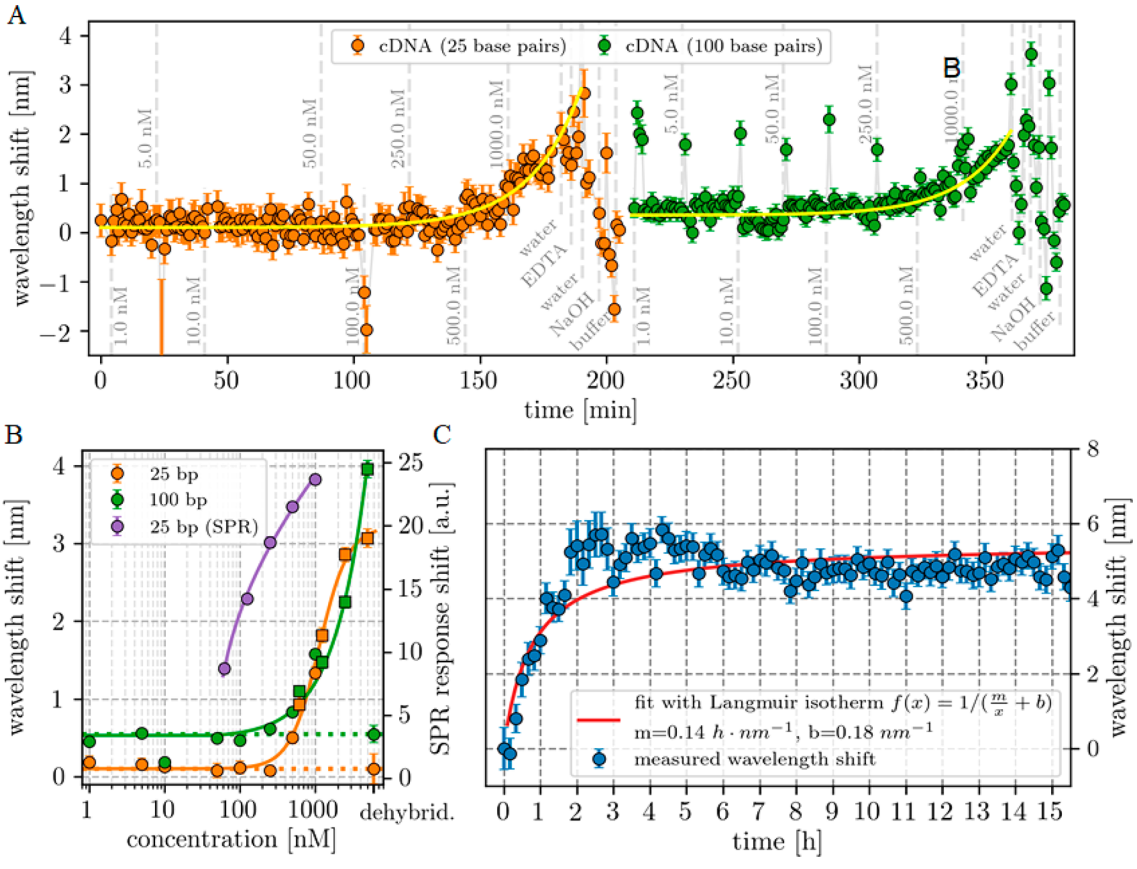

Figure 3. (A) Plasmonic response signal (wavelength shift of long-axis LSPR absorbance maximum) continuously recorded during the injection of solutions containing increasing concentrations of cDNA (25 bp and 100 bp, respectively) into the fluidic channel. Concentrations from 1 nM to 1 μM were used, with the highest concentration being followed by dehybridization. Note, the yellow lines are not an actual fit to the data, but only a guide for the eye. (B) LSPR wavelength shifts as registered in (A) [circular points], as well as in a measurement with higher concentrations (square points), plotted as a function of cDNA concentration. For both, 25-bp-long cDNA molecules, as well as 100-bp-long cDNA (red and green dots), the limit of detection is above 250 nM. For comparison, the figure shows the SPR response shift from a planar gold-layer being subject to the same hybridization procedure (blue dots). Solid lines are only intended to be a guide to the eye. (C) LSPR wavelength shift measured on a nanoantenna sample over a time period of 15 h with the nanoantennas being exposed to 10 nM cDNA solution.

DOI: 10.1021/acssensors.8b00315
ACS Sens. 2018, 3, 1392−1400

evaluation of hybridization yield occurred by reaction of rhodamine green-labeled complementary DNA. At defined time steps, the reaction was stopped by immersion of the substrates in 15 mM NaOH for at least 12 h. Noncomplementary cyanine 3 (CY3)-labeled DNA served as control measurement.

A plate reader (Tecan Infinite 200 PRO, Switzerland) was used to measure the fluorescence intensity (FI) of the samples; Table S1 contains the exact wavelength settings for each labeled DNA strand. Signals were converted into a surface coverage based on previously taken calibration curve. The corresponding results for surface coverages for immobilization of probe DNA are summarized in Table S2 and for hybridization in Table S3, respectively.

RESULTS AND DISCUSSION

Sensor Fabrication and Integration. The highly responsive nanoantennas were fabricated with an electrochemical approach as described above. As seen in Figure 1b, densely packed arrays of gold nanoantennas with a diameter of 17 nm, a length of approximately 400 nm, and a center-to-center distance of 63 nm were produced. Consequently, the gap between the nanorods measures 46 nm at the narrowest part. Figure 1b shows a SEM image of the produced nanoantenna array; the inset shows a picture of the nanoantenna array, produced on the glass substrate (without microfluidic channels) to highlight the size of arrays fabricated.

The maximum extinction at the LSPR wavelength depends on the angle of incidence of the light, which was maintained at 40° throughout the experiments described here. More specifically, the absorbance spectra show two distinct peaks indicating the excitation of a plasmon resonance along the short and the long axis of the rods. While the short-axis resonance is centered around a wavelength of 500 nm, the long axis resonance is dependent on the aspect ratio of the rods and the surrounding media, hence facilitating a tuning of the plasmon wavelength (see Figure 1c), as well as the refractometric sensing by means of monitoring the peak position (see Figure 2c).

In order to investigate the optical sensor performance and to determine reaction kinetics in real-time, an improved microfluidic setup had to be established (Figure 1a) which features not only a rapid, concise, and locally well directed delivery of small volumes of analytes to the sensing area, but also enables a synchronized reliable optical readout. For these purposes, nanoantenna substrates and thin glass slides were connected to working sensors with polydimethylsiloxane (PDMS) based microfluidic chambers in a layer-wise approach as described in ref 52. Sensors equipped with common PDMS microfluidics showed weaker and less sharp spectra under illumination. In order to overcome these scattering issues, 500-μm-thick glass slides as bottom and top barriers were used instead and produced in a multistep procedure, as described in ref 52. This geometry led to a tightly sealed microfluidic system with defined channel geometries and minimized optical signal losses that enables measuring clear spectra with pronounced peaks at all time (see Figure 3a).

Biosensing with Nanoantenna Array. The performance of nanoantenna arrays upon binding of probe, subsequent blocking and further reaction with targets were studied by means of LSPR. Absorption spectra were taken continuously to sense the binding reactions in real-time. Here, Figure 2c presents the actual absorbance spectra recorded after each reaction step including a schematic drawing of the associating surface reactions. It is evident that with each reaction step a red shift of the optical spectra occurs.

First, the response of the nanoantenna sensor toward immobilization of the probe oligonucleotides was studied. For this purpose, 5 μM probe DNA were incubated overnight in IB to ensure enough time for forming a homogeneous self-assembled oligonucleotide layer. During the immobilization, the position of the LSPR peak showed a continuous redshift of up to 1 nm within the first 5 h of reaction; afterward, a regression of the signal occurred. Fitting the data with a Langmuir isotherm suggests that equilibrium is reached at a shift of $\Delta\lambda$ = 2.1 nm (see Figure 2d). It seems reasonable to address the expected time that is needed to occupy all surface sites at the nanorod sample by a molecule. Considering Einstein's equation of diffusion, with $\langle r^2 \rangle = 6D \times \tau$, where D is the diffusion coefficient of a 25 bp ssDNA, given with 120×10^{-8} cm^2/s,[55] and r = 2 mm the maximum pathway of diffusion transport in the given geometry, the maximum diffusion time τ can be estimated to be around τ = 1.53 h. Apparently, the incubation time that is needed before the measured signal saturates significantly exceeds the maximum time needed for any diffusion-limited transport of molecules inside the fluidic chamber. Hence, we assume that the time-scale for immobilization of the initial DNA is largely dominated by the process of establishing the molecular bonding at the gold surface. The observed kinetics of the binding is in agreement with the previously published experimental results.[56,57]

It should be noted that further biodetection assays consistently resulted in a redshift of the optical signal from the nanoantenna array. After the immobilization of the initial probe DNA, backfilling with 5 mM Mercapto-1-hexanol solution was performed intended to fill vacant binding sites on the gold surface and to set immobilized DNA strands upright (see Figure 2b). Here, we take into account several reports[56,58] claiming that immobilized DNA does not bind only perpendicular to but also parallel to the surface. By treating the substrates with 6-mercapto-1-hexanol solution (MCH), the organic layer will be reorganized to a dense self-assembled monolayer by replacement of loosely bound probe DNA molecules and subsequent filling with shorter MCH[59] (Figure 2b). Consequently, a further redshift of the signal of ~2 nm within a much shorter time of only a few minutes occurred, demonstrating that the reaction took place relatively fast (see Figure 2d right panel).

Influence of Concentration and Length of DNA Fragments. Next, hybridization experiments and their kinetic responses on nanoantenna sensors were examined for two different DNA target strands, namely, 25 bp and 100 bp long. The aim of the experiments was to determine the capabilities of the designed sensor element to distinguish the binding kinetics of the molecules with different lengths, taking into account the geometry of the sensor (vertical array of nanorods) and potential complications for the longer molecular chains to penetrate into the interspaces between nanoantennas. At first, a 25-bp-long, fully complementary DNA strand (cDNA) was allowed to bind to the probe DNA. Solutions with a stepwise increase of target concentration, ranging from 1 nM to 1000 nM, were injected into the fluidic chamber in intervals of approximately 15 min while acquiring absorbance spectra at intervals of 1 min (see Figure 3a). Note that with each injection step of the cDNA-solution, we shortly observe a concurrent spike in the signal. However, it was possible to associate these with the occurrence of small air inclusions inside the channel that interfere with the optical signal while passing the illuminated area on the sample. A clear

DOI: 10.1021/acssensors.8b00315
ACS Sens. 2018, 3, 1392−1400

sensor response could be detected for the 25 bp cDNA at concentrations above 250 nM and higher, ending up to a wavelength shift of $\Delta\lambda = (1.33 \pm 0.08)$ nm at c(cDNA25) = 1 μM (compare signal in Figure 3a at ∼165 min). However, signal saturation and thus concomitant reaction equilibrium occurred only at concentrations higher than 250 nM (see Figure 3a at ∼140 min). The highest concentration was followed by initiating the dehybridization of the complementary strands, using EDTA and NaOH, for regeneration of the sensor (see signals between 180 and 200 min, respectively, in Figure 3a). As seen in Figure 3a, at around 210 min, the initial base level of the signal is restored, indicating that the dehybridization was successfully performed.

The same procedure was repeated with a set of 100-bp-long DNA strands, where only the first 25 bps were complementary to the probe strand. Here, we observe a resonance shift already above a concentration threshold of c(cDNA100) = 250 nM (see Figure 3a at 310 min), which is expected since the molar mass of the target molecule is increased. Again, the redshift accumulates with increasing the concentration of the molecules in solution, leading to a final wavelength shift of $\Delta\lambda = (1.58 \pm 0.06)$ nm for c(cDNA100) = 1 μM. Admittedly, there was barely any saturation of the signal observed, indicating that the full saturation of the receptors has not been reached. Nevertheless, the absolute signal values during hybridization with longer targets get higher compared to shorter ones after the same time of hybridization. Like before, the initial signal levels could be retrieved by a subsequent dehybridization procedure (compare time range between 360 and 400 min in Figure 3a). The detailed findings are illustrated more clearly in Figure 3b, which summarizes the concentration-dependent LSPR shifts at different concentrations showing the dynamic range, as extracted from data in Figure 3a, as well as from a second set of measurements at higher concentrations (square data points), for both target strands. For comparison, analogous hybridization experiments of both targets were performed on planar gold surfaces employing a common SPR device and are displayed as well. All respective detection curves, for nanoantenna and planar gold surfaces, for both targets are comparable as indicated in Figure 3b. In agreement, the propagating SPR signal increases with increasing target concentrations. Here, a linear behavior for rather low concentrations exists, whereas afterward a regression appeared. A similar performance of nanoantenna and planar substrates (Supporting Information, Tables 2 and 3) was seen for the influence of target length: after normalizing the signals to their maximum values, reaction kinetics for longer targets are slower than for shorter ones, whereas the overall signal change of longer targets is higher than the signal shift for shorter targets. Faster kinetics for shorter DNA strands originate from locally higher molar concentrations on the surface due to higher diffusion coefficient of smaller molecules and thus to faster reaching of equilibrium. Nevertheless, the overall molar mass of longer targets is higher, leading to higher overall changes in the local surrounding (including refractive index). Consequently, a lower detection limit can be expected for longer target strands[28] (Figure 3b). Applying a constant flow with the help of microfluidic support will cause qualitative changes in reactions since laminar flow in the channel interferes with present diffusion regimes.[60] Consequently, an enhanced mass transport will compromise the resulting limit of detection. Considering the comparatively high detection limit after short exposure times, the sensor performance was evaluated more precisely by studying the extended exposure times of up to 24 h of the chosen probe-target system. As an example, the long-time reaction with low concentrated incubation DNA and with 10 nM of 25 bp cDNA is selected: by guiding the solution over the surface with 1 μL/min, the saturation is reached after 2.5 h, as shown in Figure 3d. A clear redshift of the signal, peaking at $\Delta\lambda \sim 6$ nm after 2.5 h, before transitioning into a plateau, is evident. An approximation of the data with a Langmuir isotherm model finds the signal plateau at $\Delta\lambda = 5.6$ nm. This is in contrast to the case of high concentrations, where the target concentrations of 500 nM or higher could be detected within the first 15 min of reaction as presented in Figure 3a. Further decrease of concentration to 1 nM target achieved saturation after 24 h and vice versa higher target levels of 1 μM accelerated the reaction time to less than 3 min.

Surface Coverage and Hybridization Efficiency. In light of previous findings, the surface coverage and its progress kinetics is examined more precisely. Experimentally, fluorescent intensities of immobilization of differently concentrated probe DNA on planar and structured samples were studied and are presented in Table 1. The highest surface coverages can be seen for probe DNA with concentrations of 5 μM and 2.5 μM with close to 2.29×10^{13} and 3.09×10^{13} molecules/cm^2 at the planar gold surface, respectively. For similarly concentrated receptors on nanoantenna substrates, the surface coverage decreased to 1.09×10^{13}/cm^2 and 0.39×10^{13}/cm^2, respectively. To weigh the observed signals of nanoantenna surfaces, especially against planar gold surfaces, a rough estimation of possible accessible binding sites was made. For planar surfaces, experimentally determined surface coverages of 2.0×10^{13} up to 6.9×10^{13} molecules/cm^2 are achieved[57,61,62] steric hindrances and hydration shell around the coils will limit this value. When taking into account the curvature of structured surfaces, actually a higher immobilization efficiency is expected.[54,63] Subsequent backfilling will reduce the coverage on both substrates due to desorption of loosely bound DNA.[56] Therefore, we are interested in the particular effects of the nanorod geometry to explain the observed discrepancies to the literature values here. The rods are homogeneous in size and distribution with a diameter of 17 nm and a length of 390 nm. Due to the limited surface-to-surface-distance of 46 nm, only the upper part of the nanoantennas are considered to be available for immobilization. Thus, for a 1 mm^2 large sensor the accessible surface is given with 0.36×10^{12} nm^2, which is only a third of what is available on the same surface of a planar substrate. Accordingly, the number of bound probes is expected lower due to fewer amount of binding surface sites. The supposition is coherent with our determined surface coverage on nanoantenna substrates. Generally, the curvature of antennas still allow for high coverages on the surface. Sufficiently high surface coverages were additionally ensured by addition of $MgCl_2$ to probe strands, too. The salt minimizes electrostatic repulsion of the phosphate backbone of probe DNA.[64]

Likewise, the yield of hybridization was calculated for different target concentrations and reaction times on both substrates. For planar surfaces, the yield of hybridization of a 1 μM target increases from 12.8% to 24.7% as the hybridization time is extended from 1 h to 4 h. Strikingly, on the nanoantenna substrates, the yield increased up to 39.1% for a 1 μM target after 4 h reaction time. To check the concentration dependence, all samples were allowed to hybridize for 4 h. At low concentrations of 10 nM target,

DOI: 10.1021/acssensors.8b00315
ACS Sens. 2018, 3, 1392−1400

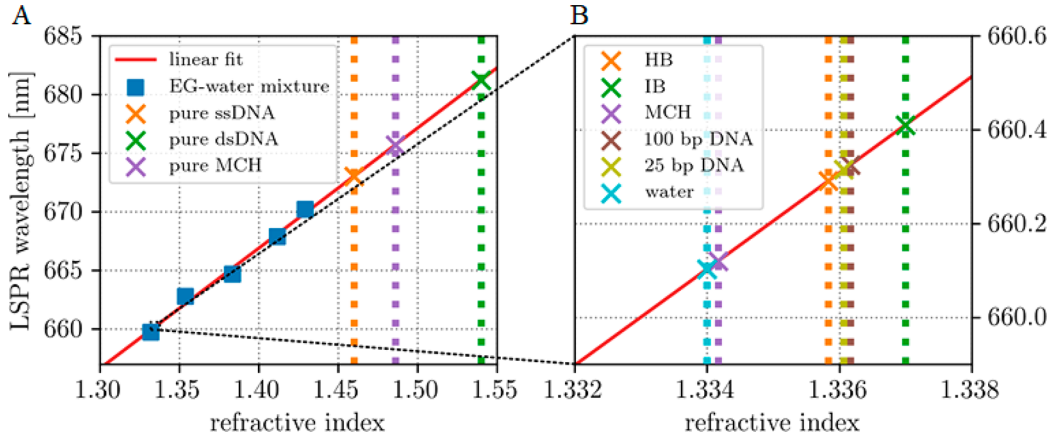

Figure 4. (A) Correlation between the spectral positions of the nanoantennas' localized surface plasmon resonance (LSPR) as determined from optical absorbance measurements (c.f. Figure 3a) and the adjusted refractive index of an ethylene glycol–water mixture inside the microfluidic channel (blue squares). (B) Experimentally determined RI values of the solutions (immobilization buffer, hybridization buffer and water, as well as MCH, 25 bp DNA, 100 bp DNA in buffer solution) used during the sensing experiment (dotted lines). Using the linear fit of the RI dependent data from the nanorod samples (red line), we can estimate the expected LSPR signal response (wavelength shift).

only 11.3% of the targets hybridized, whereas at 100 nM, the yield leveled off at 18.9%. The exact values for all measurements are summarized in Table S3. Rather low hybridization efficiencies of ~25% or less are in agreement with previous reports;[62,65] one reason behind this is the high density of probe DNA causing steric and electrostatic hindrance.[54,57,66] Overall, fewer targets than probes will bind to the surface and consequently smaller wavelength shifts of the nanoantenna sensors are expected for hybridization than for immobilization. However, the yield of hybridized DNA is higher on nanoantenna surfaces than on planar ones since they are exposed by means of their curved nature. By contrast, longer chains will limit the accessibility toward the densely packed nanoantenna arrays due to enhanced electrostatic repulsion and steric interferences between the chains and the antennas themselves.

Refractive Index Sensing. The dependence of surface plasmon resonances on refractive indices of the surroundings are known to be highly sensitive.[34,67] Inspection of the data for hybridization of 25-bp-long cDNA as well as with 100-bp-long counterpart in Figure 3b, an initial offset (with respect to the signal for a pure buffer solution) of around $\Delta\lambda$ = 0.25 nm and $\Delta\lambda$ = 0.5 nm, respectively, can be noticed at concentration levels even below the sensitivity limit. These might be connected to an increased (bulk) refractive index of the respective solution, rather than due to an actual adsorption of molecules to the surface of the sample. In order to clarify the influence of the solution's refractive index (RI) on the measurement, the RI of any bulk solution with and without DNA was determined with an ABBE refractometer at the sodium D-line of λ = 589 nm and related to spectral shifts. By acquiring transmission spectra of nanoantennas while adjusting the RI of an ethylene glycol (EG)/water mixture inside the fluidic system by means of increasing the EG volume fraction (Figure 4), the sensitivity could be calculated. Using a linear fit to the data, this measurement yields in a RI sensitivity of (102.5 ± 6.6) nm/RIU. This result can be used to estimate the LSPR wavelength for a given RI of the solution, as shown in Figure 4b. The exact values for the experimentally determined RI of buffers, calibration, and all projected shifts can be found in Table S4. Given that the difference between the RI of bulk solutions is very small, the expected wavelength shifts upon exchange of surrounding media with buffers and reaction solutions are very small, too. In the range of approximately 0.19 to 0.22 nm, these shifts are significantly smaller than the signals we measured during the hybridization experiment. On the other hand, formation of different organic layers cause continuous redshifts of the signal due to local increase of RI. Considering the RI for each layer individually, namely, single-stranded probe DNA with 1.456, backfilling agent MCH with 1.86, and double-stranded target-probe DNA complex with 1.52,[58,68] a maximum redshift of about 12.49, 15.57, and even 21.10 nm can be expected theoretically, as shown in Figure 4. This corroborates our conclusion that the measured shifts are caused by an actual agglomeration of molecules and not merely by a change of the surrounding medium's RI.

CONCLUSIONS

In summary, we investigated the biosensing performance of an extended nanoantenna array with implemented microfluidic system. Immobilization, blocking, and (de)hybridization of a short oligonucleotide onto nanoantennas were monitored by means of LSPR in real-time and compared to conventional SPR. We evaluated the performance of the sensor by applying different lengths and concentrations of target DNA. Redshifts of up to 8 nm could be detected upon functionalization with organic molecules. As demonstrated, the continuous recording of the optical spectra in this setup allows for label-free, real-time measurements inside a flow channel with high throughput and capability for multiplexed measurements. The sensors can be fabricated in large areas with defect-poor antennas in high density and defined geometry. Furthermore, the possibility to vary the aspect ratio enables the tuning of the optical properties. Thus, the performance of the sensor can be suited to any target by tailoring the aspect ratio of diameter to length; an extinction of the LSPR in the infrared spectra could be achieved and simultaneous analysis of individual molecules and their structural properties are predicted.

ASSOCIATED CONTENT

Supporting Information

The Supporting Information is available free of charge on the ACS Publications website at DOI: 10.1021/acssensors.8b00315.

DOI: 10.1021/acssensors.8b00315
ACS Sens. 2018, 3, 1392–1400

Detailed summary of the methods and techniques used for fabrication and characterization of the sensor device (PDF)

AUTHOR INFORMATION

Corresponding Author

*E-mail: larysa.baraban@nano.tu-dresden.de.

ORCID

Larysa Baraban: 0000-0003-1010-2791

Gianaurelio Cuniberti: 0000-0002-6574-7848

Present Address

[¶]M.B.: HSEB Dresden GmbH, Manfred-von-Ardenne-Ring 4, 01099 Dresden

Author Contributions

[#]The manuscript was written through contributions of all authors. All authors have given approval to the final version of the manuscript. Stephanie Klinghammer and Tino Uhlig contributed equally.

Notes

The authors declare no competing financial interest.

ACKNOWLEDGMENTS

We acknowledge experimental support by Stephan Barth (Fraunhofer-Institut für Organische Elektronik, Elektronenstrahl- und Plasmatechnik FEP) and Nicole Isserstedt-John (microfluidic ChipShop GmbH, Jena), as well as Rainer Schwierz for his assistance with experimental determination of refractive indices. In addition, we acknowledge Ms. Heike Zimmermann and Ms. Beate Katzschner for their help with measurements of the fluorescence intensities of our samples. This work was funded by the free state of Saxony via SAB/SMWK project "BioPlasNano" and the BMBF (German Ministry of Education and Research) project "PlasmoSens" (grant number 13N13732).

REFERENCES

(1) Bahadır, E. B.; Sezgintürk, M. K. Applications of commercial biosensors in clinical, food, environmental, and biothreat/biowarfare analyses. *Anal. Biochem.* **2015**, *478*, 107−120.

(2) Cetó, X.; Voelcker, N. H.; Prieto-Simón, B. Bioelectronic tongues: New trends and applications in water and food analysis. *Biosens. Bioelectron.* **2016**, *79*, 608−626.

(3) Johnson, K. S.; Needoba, J. A.; Riser, S. C.; Showers, W. J. Chemical Sensor Networks for the Aquatic Environment. *Chem. Rev.* **2007**, *107* (2), 623−640.

(4) Martinez, A. W.; Phillips, S. T.; Whitesides, G. M.; Carrilho, E. Diagnostics for the Developing World: Microfluidic Paper-Based Analytical Devices. *Anal. Chem.* **2010**, *82* (1), 3−10.

(5) Patolsky, F.; Zheng, G.; Lieber, C. M. Fabrication of silicon nanowire devices for ultrasensitive, label-free, real-time detection of biological and chemical species. *Nat. Protoc.* **2006**, *1* (4), 1711−1724S.

(6) Schütt, J.; Ibarlucea, B.; Illing, R.; Zörgiebel, F.; Pregl, S.; Nozaki, D.; Weber, W. M.; Mikolajick, T.; Baraban, L.; Cuniberti, G. Compact nanowires sensors probe microdroplets. *Nano Lett.* **2016**, *16* (8), 4991−5000.

(7) Baek, E.; Pregl, S.; Shaygan, M.; Römhildt, L.; Weber, W. M.; Mikolajick, T.; Ryndyk, D. A.; Baraban, A.; Cuniberti, G. Optoelectronic switching of nanowire-based hybrid organic/ oxide/ semi-conductor field-effect transistors. *Nano Res.* **2015**, *8* (4), 1229−1240.

(8) Medina-Sánchez, M.; Ibarlucea, B.; Pérez, N.; Karnaushenko, D. D.; Weiz, S. M.; Baraban, L.; Cuniberti, G.; Schmidt, O. G. High-performance three-dimensional tubular nanomemb-rane sensor for DNA detection. *Nano Lett.* **2016**, *16* (7), 4288−4296.

(9) Qureshi, A.; Gurbuz, Y.; Niazi, J. H. Biosensors for cardiac biomarkers detection: A review. *Sens. Actuators, B* **2012**, *171*, 62−76.

(10) Sackmann, E. K.; Fulton, A. L.; Beebe, D. J. The present and future role of microfluidics in biomedical research. *Nature* **2014**, *507* (7491), 181−189.

(11) Stephen Inbaraj, B.; Chen, B. H. Nanomaterial-based sensors for detection of foodborne bacterial pathogens and toxins as well as pork adulteration in meat products. *J. Food Drug Anal.* **2016**, *24* (1), 15−28.

(12) Viswambari Devi, R.; Doble, M.; Verma, R. S. Nanomaterials for early detection of cancer biomarker with special emphasis on gold nanoparticles in immunoassays/sensors. *Biosens. Bioelectron.* **2015**, *68*, 688−698.

(13) Zhou, W.; Gao, X.; Liu, D.; Chen, X. Gold Nanoparticles for In Vitro Diagnostics. *Chem. Rev.* **2015**, *115* (19), 10575−10636.

(14) Zhu, X.; Li, J.; He, H.; Huang, M.; Zhang, X.; Wang, S. Application of nanomaterials in the bioanalytical detection of disease-related genes. *Biosens. Bioelectron.* **2015**, *74*, 113−133.

(15) Engvall, E.; Perlmann, P. Enzyme-linked immunosorbent assay (ELISA) quantitative assay of immunoglobulin G. *Immunochemistry* **1971**, *8* (9), 871−874.

(16) Hnasko, R., Ed. *ELISA: methods and protocols*; Humana Press: New York, 2015.

(17) Olson, J.; Amolins, M.; Vitiello, P. Creating a Reliable, Cost-Effective ELISA Simulation. *Am. Biol. Teach.* **2017**, *79* (4), 301−304.

(18) Garibyan, L.; Avashia, N. Polymerase Chain Reaction. *J. Invest. Dermatol.* **2013**, *133* (3), 1−4.

(19) Mullis, K. B.; Faloona, F. A. Specific synthesis of DNA in vitro via a polymerase-catalyzed chain reaction. *Methods Enzymol.* **1987**, *155*, 335−350.

(20) Heid, C. A.; Stevens, J.; Livak, K. J.; Williams, P. M. Real time quantitative PCR. *Genome Res.* **1996**, *6* (10), 986−994.

(21) Goering, R. V. Pulsed field gel electrophoresis: A review of application and interpretation in the molecular epidemiology of infectious disease. *Infect., Genet. Evol.* **2010**, *10* (7), 866−875.

(22) Westermeier, R. Looking at proteins from two dimensions: a review on five decades of 2D electrophoresis. *Arch. Physiol. Biochem.* **2014**, *120* (5), 168−172.

(23) Kurien, B.; Scofield, R. Western blotting. *Methods* **2006**, *38* (4), 283−293.

(24) Yang, P.-C.; Mahmood, T. Western blot: Technique, theory, and troubleshooting. *North Am. J. Med. Sci.* **2012**, *4* (9), 429.

(25) Mayer, K. M.; Hafner, J. H. Localized Surface Plasmon Resonance Sensors. *Chem. Rev.* **2011**, *111* (6), 3828−3857.

(26) Jönsson, U.; Fägerstam, L.; Ivarsson, B.; Johnsson, B.; Karlsson, R.; Lundh, K.; Löfås, S.; Persson, B.; Roos, H.; Rönnberg, I. Real-time biospecific interaction analysis using surface plasmon resonance and a sensor chip technology. *BioTechniques* **1991**, *11* (5), 620−627.

(27) Nguyen, H.; Park, J.; Kang, S.; Kim, M. Surface Plasmon Resonance: A Versatile Technique for Biosensor Applications. *Sensors* **2015**, *15* (5), 10481−10510.

(28) Retra, K.; Irth, H.; van Muijlwijk-Koezen, J. E. Surface Plasmon Resonance biosensor analysis as a useful tool in FBDD. *Drug Discovery Today: Technol.* **2010**, *7* (3), e181−e187.

(29) Wang, D.-S.; Fan, S.-K. Microfluidic Surface Plasmon Resonance Sensors: From Principles to Point-of-Care Applications. *Sensors* **2016**, *16* (8), 1175.

(30) Skoog, D. A.; Holler, F. J.; Crouch, S. R. *Principles of instrumental analysis*, 6th ed.; Thomson Brooks/Cole: Belmont, CA, 2007.

(31) Mitchell, J. S.; Wu, Y.; Cook, C. J.; Main, L. Sensitivity enhancement of surface plasmon resonance biosensing of small molecules. *Anal. Biochem.* **2005**, *343* (1), 125−135.

(32) Mitchell, J. Small Molecule Immunosensing Using Surface Plasmon Resonance. *Sensors* **2010**, *10* (12), 7323−7346.

(33) de Mol, N. J. Affinity Constants for Small Molecules from SPR Competition Experiments, In *Methods Mol. Biol.*, Mol, N. J.; Fischer,

DOI: 10.1021/acssensors.8b00315
ACS Sens. 2018, 3, 1392−1400

M. J. E., Eds.; Humana Press: Totowa, NJ, 2010; Vol627, pp 101–111. DOI: .
(34) Willets, K. A.; Van Duyne, R. P. Localized Surface Plasmon Resonance Spectroscopy and Sensing. *Annu. Rev. Phys. Chem.* **2007**, *58* (1), 267–297.
(35) Evans, P. R.; Kullock, R.; Hendren, W. R.; Atkinson, R.; Eng, L. M. Optical Transmission Properties and Electric Field Distribution of Interacting 2D Silver Nanorod Arrays. *Adv. Funct. Mater.* **2008**, *18*, 1075–1079.
(36) Nerowski, A.; Opitz, J.; Baraban, L.; Cuniberti, G. Bottom-up synthesis of ultrathin straight platinum nanowires: electric field impact. *Nano Res.* **2013**, *6* (5), 303–311.
(37) Estevez, M.-C.; Otte, M. A.; Sepulveda, M. A.; Lechuga, L. M. Trends and challenges of refractometric nanoplasmonic biosensors: a review. *Anal. Chim. Acta* **2014**, *806*, 55–73.
(38) Cao, J.; Sun, T.; Grattan, K. T. V. Gold nanorod-based localized surface plasmon resonance biosensors: A review. *Sens. Actuators, B* **2014**, *195*, 332–351.
(39) Unser, S.; Bruzas, I.; He, J.; Sagle, L. Localized Surface Plasmon Resonance Biosensing: Current Challenges and Approaches. *Sensors* **2015**, *15* (7), 15684–15716.
(40) Kelly, K. L.; Coronado, E.; Zhao, L. L.; Schatz, G. C. The Optical Properties of Metal Nanoparticles: The Influence of Size, Shape, and Dielectric Environment. *J. Phys. Chem. B* **2003**, *107* (3), 668–677.
(41) Kvasnička, P.; Homola, J. Optical sensors based on spectroscopy of localized surface plasmons on metallic nanoparticles: Sensitivity considerations. *Biointerphases* **2008**, *3* (3), FD4–FD11.
(42) Otte, M. A.; Sepúlveda, B.; Ni, W.; Juste, J. P.; Liz-Marzán, L. M.; Lechuga, L. M. Identification of the Optimal Spectral Region for Plasmonic and Nanoplasmonic Sensing. *ACS Nano* **2010**, *4* (1), 349–357.
(43) Piliarik, M.; Šípová, H.; Kvasnička, P.; Galler, N.; Krenn, J. R.; Homola, J. High-resolution biosensor based on localized surface plasmons. *Opt. Express* **2012**, *20* (1), 672–680.
(44) Edwards, J. D.; Keller, F. Formation of Anodic Coatings on Aluminum. *Trans. Electrochem. Soc.* **1941**, *79* (1), 135.
(45) Diggle, J. W.; Downie, T. C.; Goulding, C. W. Anodic oxide films on aluminum. *Chem. Rev.* **1969**, *69* (3), 365–405.
(46) Masuda, H. Self-Ordering of Cell Arrangement of Anodic Porous Alumina Formed in Sulfuric Acid Solution. *J. Electrochem. Soc.* **1997**, *144* (5), L127.
(47) Masuda, H.; Fukuda, K. Ordered Metal Nanohole Arrays Made by a Two-Step Replication of Honeycomb Structures of Anodic Alumina. *Science* **1995**, *268* (5216), 1466–1468.
(48) Patrovsky, F.; Fiehler, V.; Derenko, S.; Barth, S.; Bartzsch, H.; Ortstein, K.; Frach, P.; Eng, L. M. Anodization of sputtered substoichiometric aluminum oxide thin-films for improved nanorod array fabrication. *Mater. Res. Express* **2017**, *4* (5), 055010.
(49) Fiehler, V.; Patrovsky, F.; Ortmann, L.; Derenko, S.; Hille, A.; Eng, L. M. Plasmonic Nanorod Antenna Array: Analysis in Reflection and Transmission. *J. Phys. Chem. C* **2016**, *120* (22), 12178–12186.
(50) Böhm, M.; Uhlig, T.; Derenko, S.; Eng, L. M. Mechanical tuning of plasmon resonances in elastic, two-dimensional gold-nanorod arrays. *Opt. Mater. Express* **2017**, *7* (6), 1882–1897.
(51) Kick, A.; Bönsch, M.; Mertig, M. EGNAS: an exhaustive DNA sequence design algorithm. *BMC Bioinf.* **2012**, *13*, 138.
(52) Gang, A.; Haustein, N.; Baraban, L.; Cuniberti, G. Multifunctional reversibly sealable microfluidic devices for patterned material deposition approaches. *RSC Adv.* **2015**, *5* (16), 11806–11811.
(53) Abate, A. R.; Lee, D.; Do, T.; Holtze, C.; Weitz, D. A. Glass coating for PDMS microfluidic channels by sol–gel methods. *Lab Chip* **2008**, *8* (4), 516.
(54) Demers, L. M.; Mirkin, C. A.; Mucic, R. C.; Reynolds, R. A.; Letsinger, R. L.; Elghanian, R.; Viswanadham, G. A Fluorescence-Based Method for Determining the Surface Coverage and Hybridization Efficiency of Thiol-Capped Oligonucleotides Bound to Gold Thin Films and Nanoparticles. *Anal. Chem.* **2000**, *72* (22), 5535–5541.
(55) Stellwagen, N. C.; Magnusdottir, S.; Gelfi, C.; Righetti, P. G. Measuring the translational diffusion coefficients of small DNA molecules by capillary electrophoresis. *Biopolymers* **2001**, *58* (4), 390–397.
(56) Herne, T. M.; Tarlov, M. J. Characterization of DNA Probes Immobilized on Gold Surfaces. *J. Am. Chem. Soc.* **1997**, *119* (38), 8916–8920.
(57) Peterson, A. W.; Heaton, R. J.; Georgiadis, R. M. The effect of surface probe density on DNA hybridization. *Nucleic Acids Res.* **2001**, *29* (24), 5163–5168.
(58) Wolf, L. K.; Gao, Y.; Georgiadis, R. M. Sequence-dependent DNA immobilization: specific versus nonspecific contributions. *Langmuir* **2004**, *20* (8), 3357–3361.
(59) Kummer, K.; Vyalikh, D. V.; Gavrila, G.; Kade, A.; Weigel-Jech, M.; Mertig, M.; Molodtsov, S. L. High-resolution photoelectron spectroscopy of self-assembled mercaptohexanol monolayers on gold surfaces. *J. Electron Spectrosc. Relat. Phenom.* **2008**, *163* (1–3), 59–64.
(60) Squires, T. M.; Messinger, R. J.; Manalis, S. R. Making it stick: convection, reaction and diffusion in surface-based biosensors. *Nat. Biotechnol.* **2008**, *26* (4), 417–426.
(61) Peeters, S.; Peeters, S.; Stakenborg, T.; Reekmans, G.; Laureyn, W.; Lagae, L.; Van Aerschot, A.; Van Ranst, M. Impact of spacers on the hybridization efficiency of mixed self-assembled DNA/alkanethiol films. *Biosens. Bioelectron.* **2008**, *24* (1), 72–77.
(62) Steel, A. B.; Herne, T. M.; Tarlov, M. J. Electrochemical Quantitation of DNA Immobilized on Gold. *Anal. Chem.* **1998**, *70* (22), 4670–4677.
(63) Hill, H. D.; Millstone, J. E.; Banholzer, M. J.; Mirkin, C. A. The Role Radius of Curvature Plays in Thiolated Oligonucleotide Loading on Gold Nanoparticles. *ACS Nano* **2009**, *3* (2), 418–424.
(64) Kick, A.; Bönsch, M.; Kummer, K.; Vyalikh, D. V.; Molodtsov, S. L.; Mertig, M. Controlling structural properties of self-assembled oligonucleotide–mercaptohexanol monolayers. *J. Electron Spectrosc. Relat. Phenom.* **2009**, *172* (1–3), 36–41.
(65) Gong, P.; Lee, C.-Y.; Gamble, L. J.; Castner, D. G.; Grainger, D. W. Hybridization behavior of mixed DNA/alkylthiol monolayers on gold: characterization by surface plasmon resonance and 32P radiometric assay. *Anal. Chem.* **2006**, *78* (10), 3326–3334.
(66) Wong, I. Y.; Melosh, N. A. An Electrostatic Model for DNA Surface Hybridization. *Biophys. J.* **2010**, *98* (12), 2954–2963.
(67) Yonzon, C.; Stuart, D.; Zhang, X.; Mcfarland, A.; Haynes, C.; van Duyne, R. Towards advanced chemical and biological nanosensors—an overview. *Talanta* **2005**, *67* (3), 438–448.
(68) Elhadj, S.; Singh, G.; Saraf, R. F. Optical properties of an immobilized DNA monolayer from 255 to 700 nm. *Langmuir* **2004**, *20* (13), 5539–5543.

DOI: 10.1021/acssensors.8b00315
ACS Sens. 2018, 3, 1392–1400